WELDING RESEARCH

SUPPLEMENT TO THE WELDING JOURNAL, MARCH, 1984

Sponsored by the American Welding Society and the Welding Research Council

A Fundamental Study of the Beneficial Effects of Delta Ferrite in Reducing Weld Cracking

Rationales proposed in the literature that seek to explain weld hot cracking behavior are subjected to critical evaluation based on extensive testing with five ternary alloys

BY J. A. BROOKS, A. W. THOMPSON, AND J. C. WILLIAMS

ABSTRACT. Iron, nickel, chromium ternary alloys were used to study fundamental reasons for weld cracking-microstructure relationships in austenitic stainless steels. These alloys covered a range in Cr/Ni ratios such that both primary ferrite and primary austenite weld solidification and varying weld ferrite contents could be studied.

Tests were conducted to determine the hot ductility response of a wide range of weld microstructures when subjected to simulated weld thermal cycles. The distribution of impurities in weld microstructures was determined by a scanning transmission electron microchemical analysis of impurity-doped welds. The hot cracking response of impurity-doped samples was determined by Varestraint testing.

The results of these tests, in addition to extensive microstructural examination, permitted a critical evaluation of eight proposed rationales in the literature which attempt to explain weld hot cracking behavior. It is concluded that rationales incorporating the characteristics of grain boundaries best explained hot cracking behavior, particularly with respect to complex crack paths along certain δ - γ boundaries and to reduced wetting of such boundaries by liquid films.

Introduction

Austenitic stainless steels have been developed and used under widely varying conditions. These conditions include corrosive environments, which austenitic stainless steels resist well, cryogenic temperatures where they exhibit high toughness, and elevated temperatures (to ~ 875 K, *i.e.*, 602°C or 1116°F) where they exhibit good oxidation resistance. Because of this versatility, these alloys are often found in advanced energy-generation systems. Such applications often require joining large sections, which subsequently must be highly reliable, and thus continue to stimulate research into the behavior of austenitic stainless steels under a wide range of operating conditions.

A major area of study has been the cause and nature of weld defects. Probably the most common weld defects in austenitic stainless steels are hot cracks. These weld cracks or fissures are due largely to low-melting liquid films that allow the liquated boundaries to separate under thermal and shrinkage stresses which develop during solidification and cooling.

Some Weld Microstructure Fundamentals

An understanding of the origin of weld microstructures is of fundamental importance when explaining weld cracking behavior, the topic of this paper. The weld microstructures of the AISI 300 series alloys are considerably different from the base metal. Usually at ambient temperatures, the homogeneous wrought alloys are entirely austenite, while welds contain varying amounts of ferrite which is retained at room temperature.

The origin of the weld microstructures

Based on a paper presented at the 63rd Annual AWS Convention, held in Kansas City Mo., during April 25-30, 1982.

J. A. BROOKS is with the Materials Development Division, Sandia National Laboratories, Livermore, California. A. W. THOMPSON is Professor of Metallurgical Engineering and Material Science and J. C. WILLIAMS is Dean of Engineering, Carnegie-Mellon University, Pittsburgh, Pennsylvania.

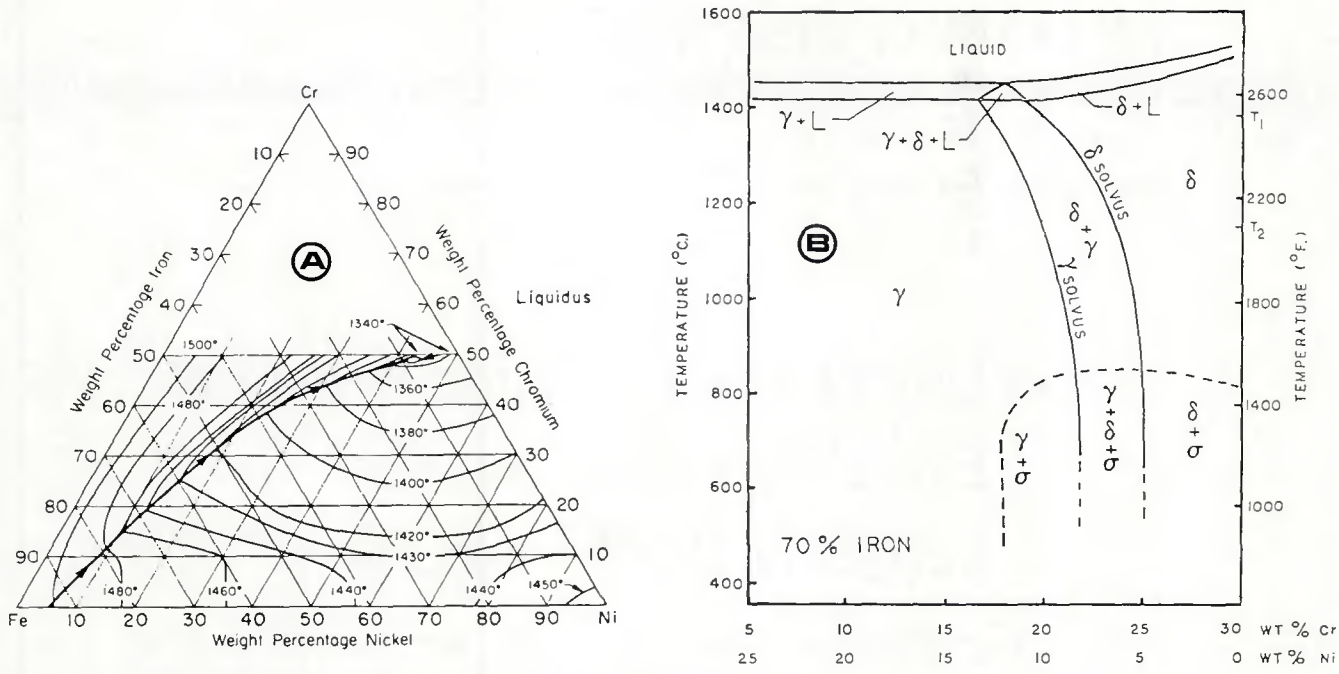

Fig. 1—Fe-Ni-Cr ternary diagram: A—liquidus surface; B—70% Fe vertical section

can best be explained with the liquidus surface of the Fe-Ni-Cr ternary diagram in Fig. 1A and the 70% constant Fe vertical section in Fig. 1B (Ref. 1). Recent work by Schurmann and Brauchmann (Ref. 2) shows that the Fe-Ni peritectic of this diagram changes to a eutectic at 75.8% Fe, 9.6% Ni, and 14.6% Cr.

Compositions on the Ni-rich side of the peritectic/eutectic liquidus, shown in Figure 1A, solidify as primary austenite, while those on the Cr-rich side generally solidify as primary ferrite (although the primary phase of solidification also depends somewhat on solidification rate). A variety of weld microstructures result and are shown schematically for a range of compositions in Fig. 2. This schematic is based partially on studies by Suutala *et al.* (Ref. 3) and others (Refs. 4-7). As Fig. 2 shows, ferrite in primary austenite solidified welds forms as a result of eutectic solidification and is distributed along solidification cell boundaries.

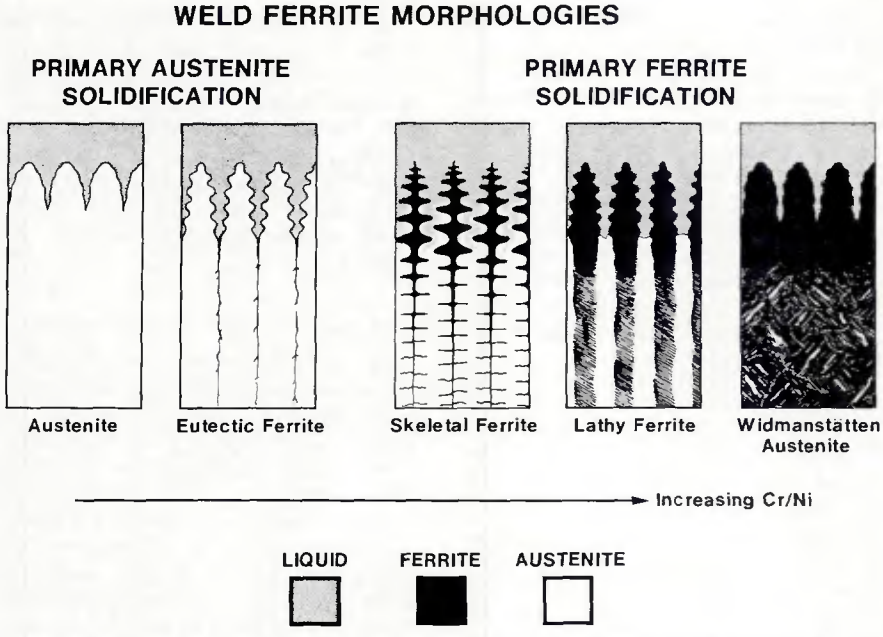

Fig. 2—Schematic of the solidification and transformation behavior resulting in a range of weld ferrite morphologies

The ferrite morphology of primary ferrite solidified welds is related to the Cr/Ni ratio (Ref. 3) and cooling rate (Refs. 4,9). These morphologies result from cooling through the ($\delta + \gamma$) phase field, shown in Fig. 1B. As shown in Fig. 2, the ferrite exhibiting the skeletal and lathy morphologies is located along the primary ferrite solidified cell cores. Austenite may also precipitate within the ferrite, forming a Widmanstätten structure. This structure usually occurs at high Cr/Ni ratios and is further promoted by high cooling rates.

A number of studies have been conducted relating the weld solidification and solid state transformation behavior to the various ferrite morphologies (Refs. 9-17). In previous studies on the solidification and solid state transformations (Refs. 11-14), extensive scanning transmission electron microscopy (STEM) analysis has shown that the primary ferrite structures in Fig. 2 result from microsegregation during solidification followed by diffusion-controlled solid state transformations upon cooling. During the transformation, Cr partitions to the ferrite and Ni to the austenite.

It has been known for many years that alloy compositions which lead to some retained ferrite in the weld deposit are much less susceptible to hot cracking than compositions which are completely austenitic. In 1938, Scherer *et al.* (Ref. 18) filed a patent which claimed that crack-

resistant weld deposits could be made if the alloy composition was balanced to produce weld deposits with 5 to 35% ferrite. Recognition of the potency of ferrite in eliminating weld cracking has resulted over a period of years in the development of empirical diagrams for predicting weld ferrite content from alloy composition (Refs. 19-21).

In an extensive study published by Hull in 1967, the cast-pin tear test was used to relate ferrite content to hot cracking (Ref. 22). His work did more than show the beneficial effect that 5 to 30% ferrite has in preventing cracking; it also demonstrated the interesting point that, at still higher levels of ferrite, crack sensitivity again increased.

Over the last decade it has been shown in a number of studies that different grades of stainless steel require different levels of ferrite to reduce cracking (Refs. 23-25). Also, several studies have indicated, at least in primary austenite solidified welds, that as the concentration of the impurity elements P and S increases, more ferrite is required to prevent cracking (Refs. 23,24,26-28), at least up to a certain level.

Only in the last five to ten years has it become generally accepted that welds (Refs. 24,5,29,3,6,9), like castings (Ref. 4), can solidify with the primary phase being either ferrite or austenite. It is also becoming more generally accepted that primary ferrite solidified welds are more crack-resistant than primary austenite solidified welds (Refs. 5,10,22,24,29). However, primary ferrite solidified welds also contain more ferrite than welds that have solidified as primary austenite.

Rationales for the Beneficial Effect of Ferrite

A number of rationales have been proposed to explain the beneficial effect of ferrite, or primary ferrite solidification, in reducing weld cracking. Several of these have been explained in some detail by previous investigators (Refs. 22,24), and so are only briefly described here. Some rationales are so general that even the source of the original suggestion has been lost in the literature. These rationales are discussed individually in the Discussion. The rationales are:

1. The higher solubility of harmful impurities in ferrite than austenite results in less segregation (Refs.23,5,7) during primary ferrite solidification than primary austenite solidification. It is the impurities, segregated to high concentration levels, which result in liquid film formation and weld cracking.

2. The ductility of ferrite at high temperatures is greater than that of austenite, allowing relaxation of thermal stresses.

3. The thermal expansion coefficient of ferrite is less than austenite. This fact results in less thermal contraction on cooling of primary ferrite solidified welds, thus reducing the tendency for fissures or crack formation during the last stages of solidification (Ref. 30).

4. The solidification temperature range of primary ferrite welds is less than that of primary austenite solidified welds. This difference reduces the critical temperature range for crack formation, in which stresses are increasing in the presence of liquid films.

5. Partitioning of minor alloying elements during primary solidification can result in synergistic behavior affecting cracking. During the solidification of ferrite, for example, Si may be less segregated to cell boundaries where it promotes liquid film formation, whereas Mn segregates to the cell boundaries where it reacts with S to form solid MnS, thus reducing the tendency for liquid sulfide film formation (Refs. 7,24,31).

6. The presence of ferrite results in a larger internal surface area due to the δ-γ interfaces. This increased area disperses the impurities which tend to segregate at interfaces and reduces high concentrations which otherwise could result in the formation of liquid phases.

7. Ferrite-austenite boundaries are not wetted by liquid films as are ferrite-ferrite and austenite-austenite boundaries. Therefore, they act as solid links until final solidification, preventing the formation of fissures (Ref. 22).

8. Cracks are arrested by the difficulty of propagation along a path of irregular ferrite-austenite boundaries rather than along rather smooth single-phase boundaries (Ref. 25). Matsuda *et al.* (Ref. 32) suggested that these irregular boundaries occur during "the peritectic/eutectic reaction." As discussed below, however, the peritectic/eutectic transition is not necessary for the generation of irregular boundaries. Alternative origins are presented.

In the study reported in this paper a large number of critical experiments were conducted and analyzed to determine which rationale most consistently explains weld cracking behavior.

Materials

Studies were conducted on 23 kg (50.7 lb) vacuum-induction-melted Fe-Ni-Cr ternary heats of compositions listed in Table 1. The alloys, with designation corresponding to the nominal Cr and Ni contents respectively, were selected to provide a variation in both solidification mode and ferrite content.

Table 1—Ternary Alloys

Alloy no.	Composition, Wt-%[a]					
	Cr	Ni	Fe	Si	C	N
19-11	18.67	11.34	70.0	0.008	0.009	0.003
23-12	22.81	11.92	65.2	0.010	0.010	0.004
22-13	21.87	13.05	65.0	0.010	0.016	0.003
21-14	21.07	14.18	64.7	0.010	0.006	0.001
10-30	10.16	30.00	40.2	0.025	0.003	0.003

(a) P = 0.002-0.006; S = 0.002-0.004.

Table 2—Ferrite Contents and Cr_{eq}/Ni_{eq} Ratios of Ternary Alloys

Alloy no.	Ferrite number, FN		Cr_{eq}/Ni_{eq}[a]
	Weld	Plate	
19-11	3.2	0	1.60
23-12	21	7.4	1.85
22-13	8.5	1.5	1.68
21-14	0.5	0	1.51
10-30	0	0	0.34

(a) 30 × (N + C) used in Ni_{eq}

Table 2 lists the Cr/Ni ratios, the phase of primary solidification of gas tungsten arc (GTA) welds on 9.5 mm (0.37 in.) thick plate made at 200 amperes (A), 14 volts (V), and 13 cm/min (5.12 in./min). The ferrite content was measured with a Magne Gage (Ref. 33). Alloys 10-30 and 21-14 solidified as primary austenite, while alloys 22-13 and 23-12 solidified as primary ferrite. Alloy 19-11 solidified in a mixed mode — that is, some regions solidified as primary austenite and others as primary ferrite, often in adjacent grains.

Ternary heats were doped with P and S to study impurity segregation. FeS and FeP reagent-grade powders were added to drilled holes in cubes weighing 10 grams (0.35 oz). The samples were weighed before and after the addition, arc melted in an Ar atmosphere, and cast into Cu crucibles. Cooling rates of the small castings were 350-500°C/s (662-932°F/s), similar to that experienced by the fusion zone of GTA welds (Ref. 34). The technique is reported in more detail elsewhere (Ref. 11).

Experimental Procedures

Samples for light metallography were etched with the following mixture: ⅓ HCl, ⅓ HNO_3, ⅓ acetic acid. Foils for transmission electron microscopy (TEM) and STEM analysis were thinned by jet

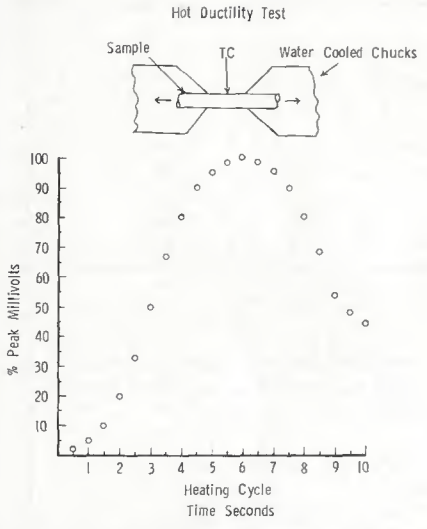

Fig. 3—Gleeble thermal cycle used in hot ductility testing. "Millivolts" are thermocouple (TC) output

polishing with a solution of 275 ml methyl alcohol, 175 ml butyl alcohol, and 30 ml perchloric acid at −50°C, *i.e.*, −58°F (Ref. 35). A JEOL JEM 120 CX microscope was used for TEM and STEM microanalysis.

Hot ductility testing was conducted on a Model 1500 Gleeble. Specimens gripped with a 2 cm (0.79 in.) jaw separation were pulled on-heating at a maximum temperature, which was reached in 8 s. Both ductility, measured by reduction of area (RA), and ultimate tensile strength (UTS) were determined. The zero strength temperature (ZST), the temperature at which the fracture load dropped to zero, was also established from these tests. In addition, experiments were conducted on-cooling after being heated to within 10°C (18°F) of the ZST. All tests were conducted at a crosshead speed of 15 cm/s (5.9 in./s). Figure 3 shows the thermal cycle, which is typical of GTA welds in stainless steel (Ref. 34).

Spot Varestraint (Refs. 36,37) testing was conducted on the ternary heats which were doped with different levels of P and S. A hole 1.6 mm (0.062 in.) diameter and 1 mm (0.039 in.) deep was drilled in the center of the 2.22 × 0.64 × 15.24 cm (0.87 × 0.25 × 6 in.) test specimens. The holes were filled with either FeS or FeP powders. The amount of impurity was determined by weighing the sample before and after the powder addition. Using manual GTA welding at low current, the powders were fused into the specimen. This weld was only ~10% the size of the final Varestraint spot weld. Impurity contents were estimated from the weight of the powder addition and Varestraint test weld volume.

Varestraint tests were conducted with a delay time chosen so that the ram struck the sample 50 milliseconds (ms) after the welding arc was extinguished. The welding time was 10 s at 125 A and 14 V, with Ar shielding. The length of weld cracking, almost exclusively in the fusion zone, was measured under 30X and 60X magnification.

This test is typically used to determine heat affected zone (HAZ) cracking susceptibility (Refs. 36-38). However, the technique also proved to be suitable for determining the nature of the weld fusion zone cracks and for the effects that impurity content, alloy composition, and weld structure have on cracking susceptibility. The impurity distribution was uniform on a macroscale and was similar to that observed in the small castings and impurity-doped weldments. When obvious crater cracks were observed, however, they were not included in the total fusion zone crack count. Crater cracks were observed only in alloys 10-30 and 21-24 with high levels of P.

Results

A variety of experiments were conducted to determine which, if any, of the rationales described in the Introduction could explain weld cracking behavior. The results of these experiments are summarized below and commented upon in the Discussion.

Hot Ductility Testing

On-heating and on-cooling tests were conducted on the five ternary heats listed in Table 1 to determine if a correlation exists between elevated temperature properties, microstructure, and weld cracking behavior of the impurity-doped alloys. The on-heating and on-cooling RA and UTS of alloy 21-14 are shown in Fig. 4.

As is shown, alloy 21-24 maintained excellent strength and ductility to the measured zero strength temperature (ZST) of 1400°C (2552°F). Both properties quickly recovered upon cooling from 10°C (18°F) below the ZST, a behavior characteristic of alloys resistant to HAZ weld cracking (Refs. 36,38). This alloy is completely austenitic to the solidus temperature. Fracture occurred by microvoid coalescence (MVC) except at the very high temperatures where intergranular fracture occurred, resulting in low values of RA. Similar fracture behavior was observed in alloy 10-30.

Alloy 23-12 also exhibited good on-heating and on-cooling strength and ductility—Fig. 5. This alloy composition, being on the Cr-rich side of the ternary peritectic/eutectic trough, experiences a solid state transformation upon being heated or cooled through the ($\delta + \gamma$) two-phase region. This is also true for alloy 23-12.

The microstructures of the as-received

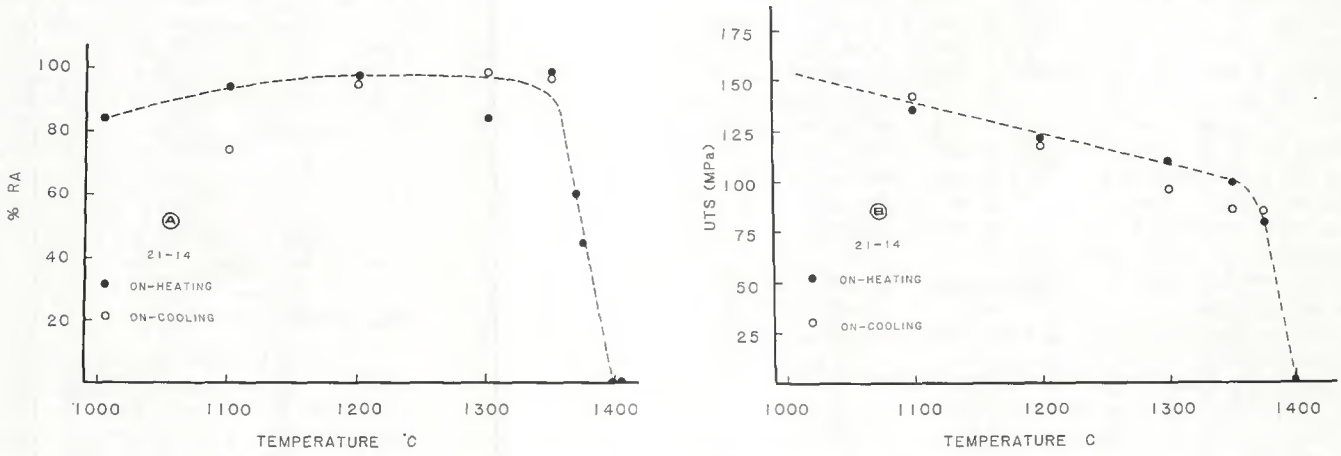

Fig. 4—Gleeble data of alloy 21-14: A—ductility results—reduction of area; B—ultimate tensile strength

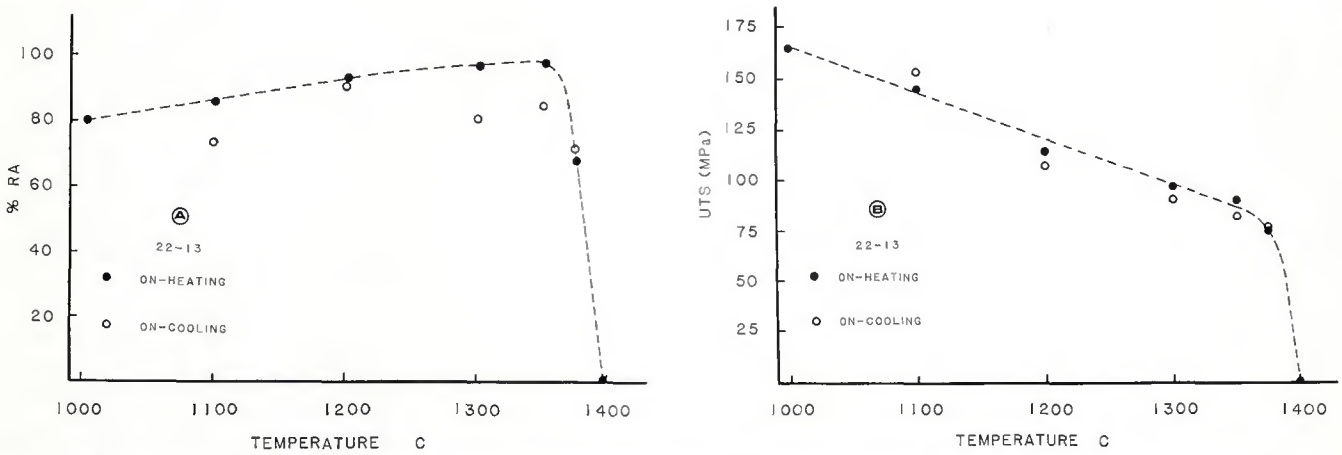

Fig. 5 — Gleeble data of alloy 22-13: A — ductility results — reduction of area; B — ultimate tensile strength

Fig. 6 — Light micrographs of Gleeble samples of alloy 23-12 heated to peak temperatures of: A — as-received; B — 1300°C (2372°F); C — 1375°C (2507°F)

alloy 23-12, a sample heated to 1300°C (2372°F), and a sample heated to 1375°C (2507°F), are shown in Fig. 6. The wrought material (Fig. 6A) has a ferrite content of FN 8. The micrograph of Fig. 6B indicates that the quantity of ferrite has increased upon heating into the two-phase region. Upon cooling some interface breakdown has occurred, resulting in regions of a lathy ferrite morphology (Ref. 14). At 1375°C (2507°F), the structure was likely all ferrite, a large fraction which has transformed to the lathy and Widmanstätten structure — Fig. 6C. The microstructures of Fig. 6, although obtained from heating inhomogeneous plates, are characteristic of those observed in weld fusion zones (Refs. 3,9,13-15) — Fig. 2.

The on-heating UTS and RA data for all the alloys are collected in Fig. 7; all the alloys maintain good strength and ductility to near the ZST. All also exhibit good recovery in strength and ductility when cooled from slightly below the ZST, similar to the results in Figs. 4 and 5.

All the alloys failed by MVC at high ductility values and by intergranular fracture at low values of RA. However, in samples which appeared to exhibit a two-phase ($\gamma + \delta$) structure near the ZST, the intergranular cracks were often arrested at the ferrite stringers — Fig. 8. In this case it is possible that no nearby transverse boundaries were available to provide a path for further crack advance.

Primary Ferrite Solidified Structures

GTA welds of alloy 22-13 and regions

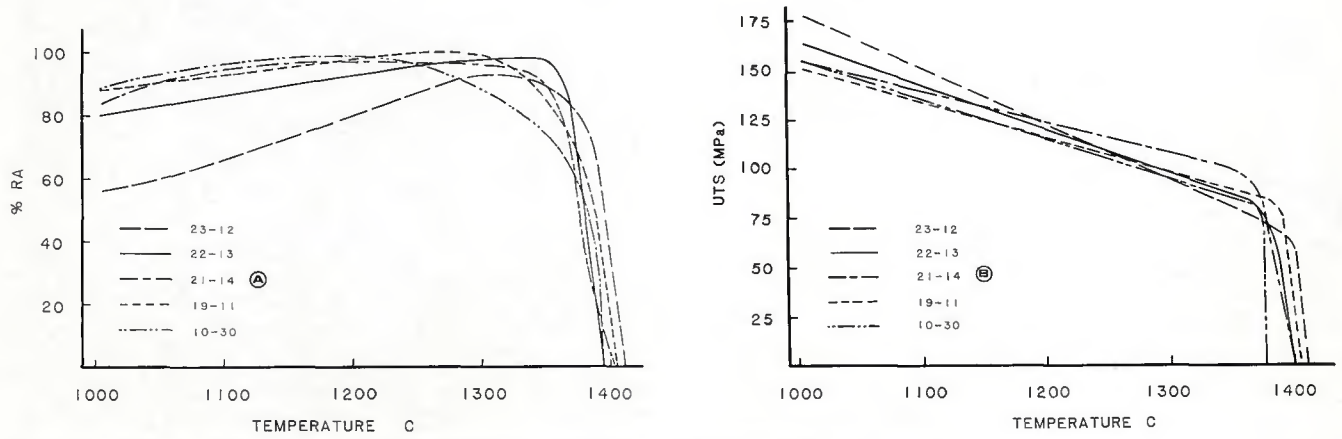

Fig. 7 — On-heating results of all ternary alloys studied: A — ductility results; B — strength results

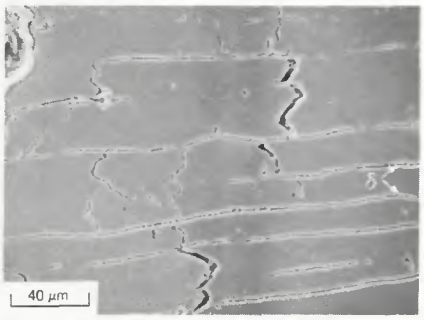

Fig. 8—Intergranular fracture of Gleeble sample of alloy 19-11 tested at 1375°C (2507°F)

of alloy 19-11 solidified as primary ferrite and exhibit primarily the skeletal ferrite morphology. No low-index orientation relationship was observed in TEM between the skeletal ferrite and austenite. However, quite often it was observed that <100>* directions of both ferrite and austenite were along the primary ferrite dendrite axis.

Figure 9A shows a skeletal ferrite dendrite, while Fig. 9B shows a higher magnification view of the ferrite-austenite boundary. Interface dislocations, similar to those in Fig. 9B, were always observed, suggesting that the $\delta + \gamma$ interfaces have a "special" character, at least partly coherent.

TEM electron diffraction (Refs. 11,13,14) studies of the lathy ferrite structures showed Nissiyama-Wasserman (NW) (Refs. 39,40) and Kurdjumov-Sachs (Ref. 41) orientation relationships. These relationships have also been reported by other investigators (Ref. 42). Both orientation relationships can lead to low-energy boundaries between ferrite and austenite.

**<100> is a crystallographic direction expressed in Miller indices.*

Figure 10A is a TEM micrograph of a partially developed lathy structure along a solidification cell. As shown in the diffraction patterns of Fig. 10B, this structure exhibits the NW orientation relationship. Also, the <100> easy growth directions of the ferrite and austenite are nearly parallel along the apparent solidification direction. The development of these structures and the relationship between solidification and solid state transformations have been reported in more detail elsewhere (Refs. 10,13,14).

Impurity Partitioning

Here, impurity partitioning is briefly described as it relates to weld cracking behavior. All master alloys were doped with high levels of P and S to determine the degree of partitioning between ferrite and austenite and the nature and distribution of impurity-containing phases.

Primary Austenite Solidification. Spherical sulfides were observed along solidification cells and austenite grain boundaries of sulfur-doped primary austenite solidified structures. These particles, shown in the light micrograph of Fig. 11, were identified by electron diffraction and STEM-EDS (energy dispersive spectroscopy) analysis as CrS. Sulfur was undetectable by EDS in ferrite and austenite because of limited solubility and detection limitations.

Unlike sulfur, which had a tendency to form liquid droplets (Fig. 4.4.9 in Ref. 11), phosphorus formed liquid films along austenite grain boundaries. However, spherical particles formed along cell boundaries in the absence of large-angle grain boundaries. EDS and electron diffraction indicated that the particles were Cr_3P. Unlike sulfur, however, phosphorus was detected in solid solution in ferrite and austenite, and was always greater in the ferrite phase.

Figure 12 shows a STEM micrograph of eutectic ferrite with 100-200 nm (3.9-7.8 × 10^{-6} in.) phosphide particles decorating the ($\gamma + \delta$) interphase boundary. The EDS spectrum in Fig. 12B, taken from the interphase particle, clearly shows the presence of phosphorus. The spectrum in Fig. 12C was taken from a 200 nm (7.8 × 10^{-6} in.) square region in the center of the ferrite. This spectrum, normalized by the Fe peak since the Fe content is similar in both phases, is compared in Fig. 12D with an austenite region adjacent to the ferrite. The concentration of phosphorus in the ferrite is considerably greater than in the austenite.

Primary Ferrite Solidification. In primary ferrite solidified structures doped with sulfur, CrS particles were observed mainly along cell boundaries. However, it appeared in some cases that sulfide droplets were also entrapped within the primary ferrite solidified structure, possibly at the onset of peritectic solidification. In all particle locations observed—grain boundaries, interphase boundaries, and solidification cell boundaries—the sulfides were of near-spherical morphology. An example of this structure, Fig. 13A, shows sulfide particles in cell boundaries, and pinning the $\gamma - \delta$ interphase boundary possibly near the region of the onset of peritectic solidification. Again, sulfur could not be detected in solid solution in either the ferrite or austenite.

Much less Cr_3P was observed in primary ferrite solidified structures than in primary austenite solidified structures at equivalent levels of doping. STEM EDS analysis also showed higher levels of phosphorus in ferrite than in the austenite. The highest phosphorus contents were often observed in the ferrite near the $\gamma - \delta$ interphase boundary. Phosphide particles were also observed at the higher levels of P (0.2%), along the interphase boundaries of skeletal ferrite.

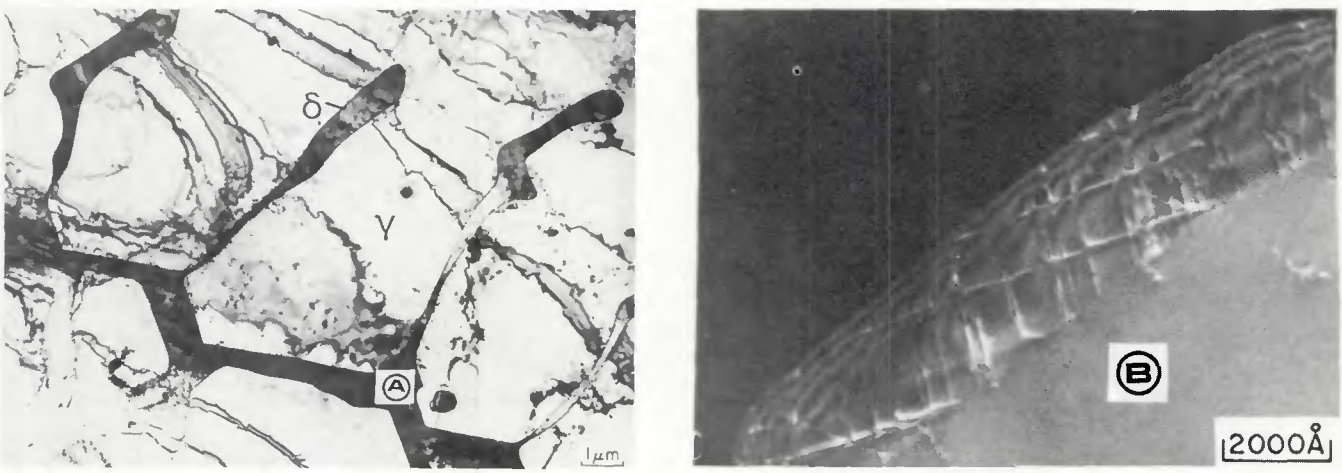

Fig. 9—TEM micrographs showing: A—skeletal ferrite along a solidification cell core; B—higher magnification of $\delta - \gamma$ interphase boundary

These observations are consistent with P partitioning to the ferrite during the $(\gamma - \delta)$ solid-state transformation, eventually reaching high enough levels to precipitate phosphides during cooling. Examples of small phosphide particles along the skeletal $\gamma - \delta$ interphase boundaries are shown in Fig. 13B.

Varestraint Test Results

Tests were conducted at a constant augmented strain, with the independent variable being impurity concentration. Two strains were used: 1% for alloys 10-30 and 21-14 and 3% for the remaining alloys. Different strains were required because of large differences in cracking susceptibility of the different alloys. For example, at 3% strain alloy 10-30 exhibited 5.1 mm (0.20 in.) total crack length with no impurity addition, while alloy 22-13 exhibited only 0.2 mm (0.008 in.) crack length with an addition of 0.08% phosphorus. Preliminary results used to establish the testing procedure are shown in Table 3.

The effect of sulfur on fusion zone cracking is shown in Fig. 14A for all the alloys studied. Alloy 10-30, which solidifies as austenite with no eutectic ferrite, exhibited the greatest degree of cracking at all levels of sulfur. Alloy 21-14, which solidifies as primary austenite but contains ~0.5% eutectic ferrite, exhibited considerably less cracking than alloy 10-30; however, it exhibited more cracking than the other three alloys, which solidify as primary ferrite and contain considerably more delta ferrite. The difference in the cracking behavior of the primary ferrite and primary austenite solidified alloys is larger than may appear in Fig. 14A due to the two different strain levels. Alloy 19-11, which solidifies in a mixed mode, was somewhat more susceptible to cracking than alloys 22-13 and 23-12 at levels of sulfur up to 0.1%.

The Varestraint results of alloys doped with phosphorus are shown in Fig. 14B. Clearly, alloys 10-30 and 21-14 are much more susceptible to cracking than the others tested. Like alloys 22-13 and 23-12, alloy 19-11 was extremely resistant to cracking except at the highest levels of phosphorus. In this case, large cracks formed along grain boundaries of primary austenite solidified regions. The majority of cracks in alloy 19-11, which solidified in a mixed mode of primary ferrite and primary austenite, occurred in the primary austenite solidified regions.

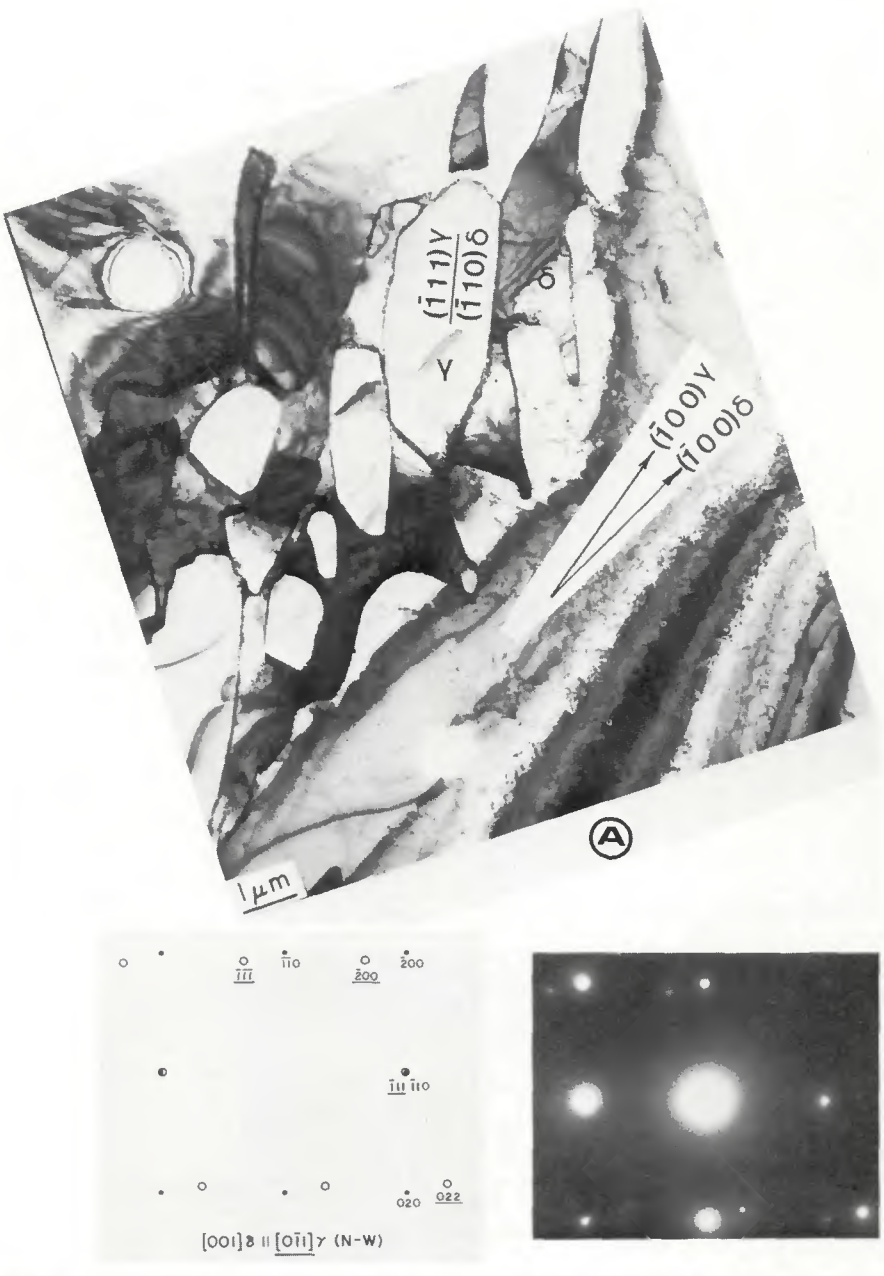

Fig. 10—TEM micrograph of lathy ferrite: A—in a weld of Alloy 22-13; B—indexed electron diffraction pattern. Note NW orientation relationship and (100) direction of ferrite and austenite along the apparent solidification direction

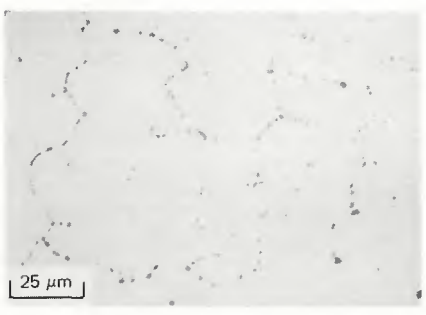

Fig. 11—Light micrograph of CrS particles along primary austenite solidification cell boundaries

Weld Crack Characterization

Primary Austenite Solidification. The nature of cracking was similar whether doping was done with phosphorus or sulfur, and it always occurred along austenite grain boundaries. At high levels of phosphorous, however, the cracks were very long and ran in some cases from near the HAZ to near the center of the weld.

Figure 15A shows an example. Here cracking occurred along the rather straight, ferrite-free grain boundaries of the columnar structure. These extremely long cracks were not formed in samples with less than 0.05% phosphorus or at any level of sulfur tested.

At the lower levels of phosphorus, the more typical cracks were similar to the one shown in Fig. 15B. The crack is clearly

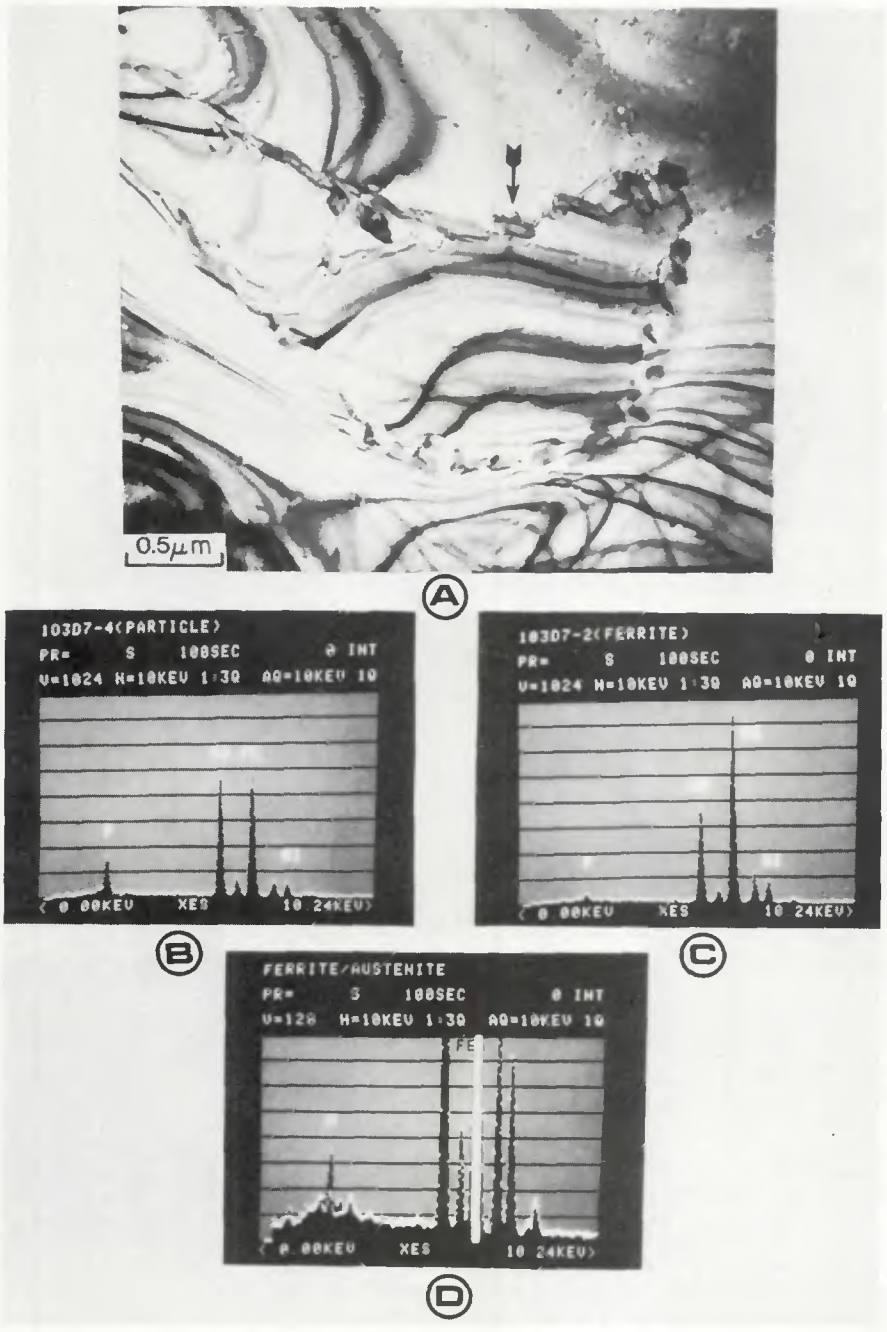

Fig. 12—Eutectic ferrite of alloy 19-11 doped with 0.3% P. A—STEM image. EDS spectra of: B—particles along δ − γ boundary; C—ferrite; D—ferrite-austenite overlay-ferrite black

Fig. 13—TEM micrographs of impurity containing particles: A—sulfides in alloy 23-12 doped with 0.24% S (note: Sulfides are along the cell and interphase boundaries of the skeletal ferrite); B—phosphides along the skeletal ferrite-austenite interface—alloy 22-13 with 0.2% P

associated with an austenite grain boundary. Also visible are two grain boundaries which did not crack. The one directly below the crack appears to have been partially liquated. Also visible are phosphide particles decorating the solidification cell boundaries.

At high levels of phosphorus the phase responsible for cracking was readily observable as shown in Fig. 15C. This phase was found from SEM-EDS analysis to be enriched in chromium and phosphorus, in agreement with the STEM analysis. The phase forming the spherical droplets along the cell boundaries is the same as that along the grain boundaries. The only difference is that the liquid droplets in the cell boundaries have no grain boundary surfaces to wet, as does the liquid segregated at the austenite grain boundaries. Also, it was observed that the phosphide liquids wet the austenite grain boundaries to a much larger degree than the sulfide liquids. This difference in wetting explains the more detrimental effect observed from phosphorus additions than with sulfur additions.

Figure 16 shows a light micrograph of a Varestraint specimen of alloy 21-14 (containing 0.5% eutectic ferrite) doped with ~0.05% phosphorus. The large crack evidently extends along an austenite grain boundary. These cracks are not as straight and smooth as the cracks in the ferrite-free weld (Fig. 15) and are likely to propagate with more difficulty. An uncracked austenite grain boundary separating the two grains below the cracked boundary (Fig. 16) is also visible; this boundary is wavy compared to that of Fig. 15B. It appears that the small amount of eutectic ferrite is effectively pinning the boundaries and preventing them from straightening.

Primary Ferrite Solidification. Figure 17 shows several cracks typical of the primary ferrite solidified alloy 22-13. The microstructure is typical of the outer region of the weld where cracking resulted. At the left in Figure 17A there is a crack along a

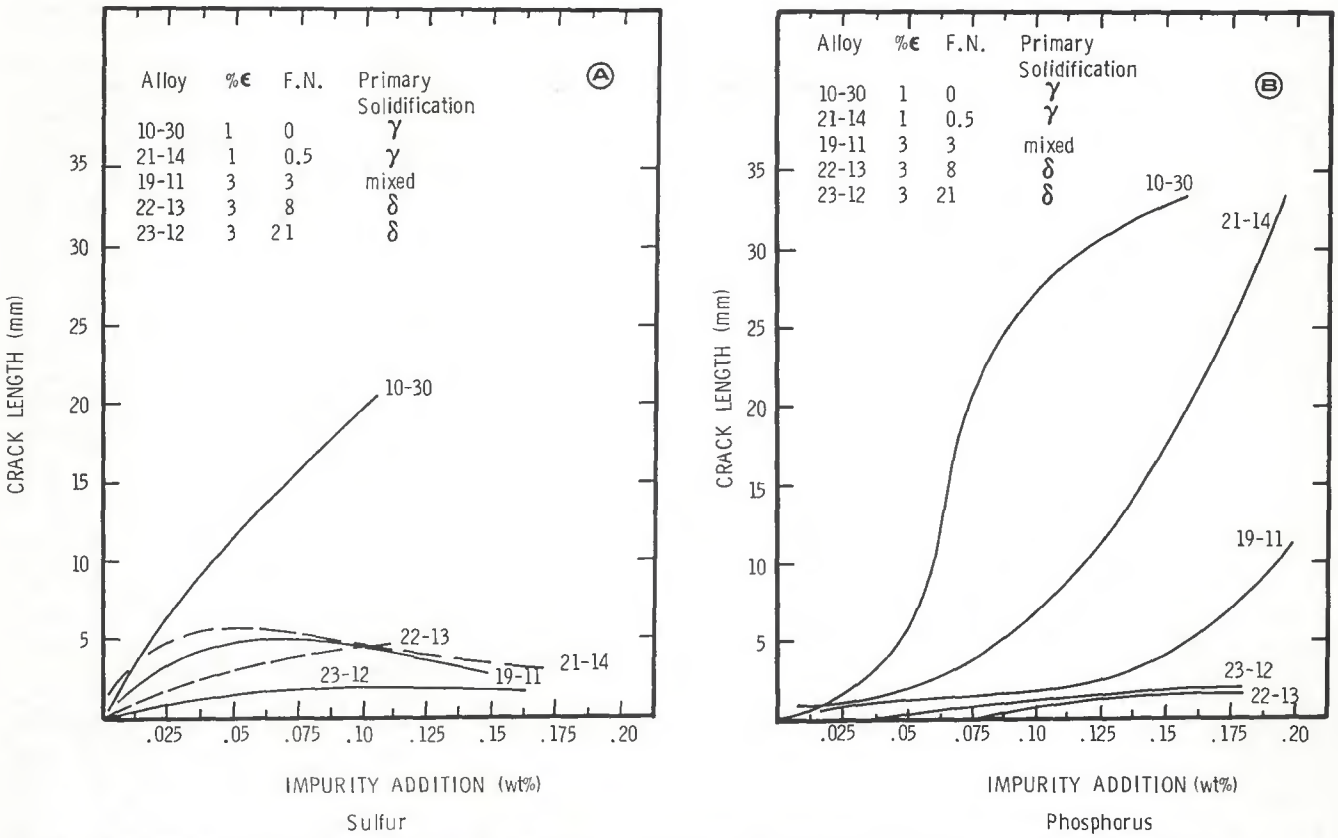

Fig. 14 — Varestraint results of doped alloys (note: two different augmented strains were used): A — S-doped alloys; B — P-doped alloys

grain boundary adjacent to a region of lathy ferrite. Also visible to the right are several other cracks. A micrograph at higher magnification of the same region is shown in Fig. 17B. Close examination shows a grain boundary on the upper side of the lathy ferrite region, and also possibly grain boundaries extending from the larger cracks in the lower region of the micrograph. The cracks are short and wide, indicating the large amount of strain required for their formation. Also, in Figure 17A it is difficult to discern the grain boundaries. As discussed later, this is the result of their incorporation along ferrite-austenite boundaries.

Alloy 23-12 was also extremely resistant to cracking. Figure 18A shows a phosphide stringer, along an apparent grain boundary region, resulting from an addition of ~0.2% phosphorus. This region nevertheless resisted cracking. A very short blunt crack, typical of those that did form in this alloy, is shown in Fig. 18B. It appears that this crack extends along a row of sulfide particles of this heavily doped specimen (~0.16% S).

Discussion

The results are discussed mainly as they relate to weld cracking behavior and to the various suggested rationales for the beneficial effect of ferrite.

One of the most commonly cited explanations of the beneficial effect of ferrite is rationale no. 1 dealing with the increased solubility in ferrite of detrimental impurities such as phosphorus and

Table 3—Varestraint Results Used to Establish Test Strains

Alloy	Strain, %	Addition, wt-%	Crack length, mm
10-30	1	0	0.58
	3	0	5.1
21-14	1	0	0
	3	0	3.7
19-11	1	0.12S	0
	1	0.17P	0
22-13	1	0.15P	0
	3	.08P	0.22
23-12	1	0.11S	0
	1	0.1P	0

Fig. 15 — Cracking of doped Varestraint specimens: A — Cracks in ferrite-free primary austenite-solidified alloy 10-30 — 0.15% P, 3% strain; B — ~0.5% P, 1% strain (note smooth cracks and austenite grain boundaries); C — ~0.15% P, 1% strain (note phosphide film associated with cracking)

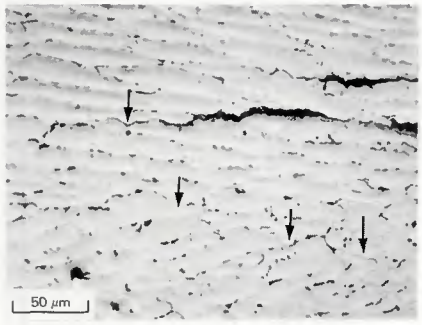

Fig. 16—Cracks in a Varestraint specimen of alloy 21-14 containing ~0.5% eutectic ferrite, doped with ~0.05% P, 1% strain. Note irregularity of crack path and austenite boundaries

sulfur. It was observed that less phosphorus was rejected during primary ferrite solidification than during primary austenite solidification.

In all cases examined, measured phosphorus levels were considerably higher in ferrite than austenite. This was observed in eutectic, skeletal, and lathy ferrite structures. Also, a larger volume fraction of phosphides in cell boundaries was observed in primary austenite structures than those of primary ferrite, for equivalent levels of doping. These observations are consistent with rationale no. 1 in the Introduction.

It was also shown that sulfur as sulfides was less segregated to cell boundaries of primary ferrite solidified structures than those solidified by primary austenite. However, in addition to the differences in solubility, another possible reason for the reduced number of sulfides in cell boundaries is sulfide entrapment between the ferrite dendrite arms during primary ferrite solidification. Such sulfide entrapment, with the addition of possible entrapment along $\gamma - \delta$ phase boundaries at the onset of peritectic solidification, would also result in less sulfides at cell and austenite grain boundaries—Fig. 13A.

Even when doped with extremely high levels of phosphorus and sulfur where large quantities of phosphides and sulfides were visible within the microstructure (demonstrating that both ferrite and austenite must have been saturated with phosphorus or sulfur), the primary ferrite solidified structures were very resistant to weld cracking. These results indicate that, although there was less tendency for phosphorus and sulfur partitioning in primary ferrite solidified structures, the increased solubility of phosphorus and sulfur in ferrite cannot explain the much higher degree of cracking resistance of primary ferrite solidified welds. These results thus provide strong evidence that rationale no. 1 cannot explain the cracking behavior, even though the segregation it describes does occur.

Rationale no. 2 suggests differences in properties between ferrite and austenite. However, it cannot explain the large observed differences in cracking behavior. The Gleeble results of Fig. 7 show that the elevated temperature strength and ductilities of all heats are very similar, contradicting rationale no. 2. Also, no obvious transition in properties resulted upon heating or cooling through the different phase fields (for example, in alloy 23-12), although this rationale would predict such a transition.

Rationale no. 3, which is based on the lower thermal expansion of ferrite than austenite, may seem attractive now that it is recognized that a larger amount of ferrite is present at elevated temperatures than is observed at room temperatures. However, the large strains applied during Varestraint testing, which still resulted in little cracking, largely overrode the effect of the differences in thermal expansion. Alloys solidified as primary ferrite and subjected to 3% applied strain were much more resistant to cracking than alloys solidified as primary austenite, but only subjected to 1% applied strain—Table 3. The difference in testing strain level is much greater than can be accounted for by differences in thermal expansion coefficients. Furthermore, alloys which solidify completely as ferrite are also susceptible to weld cracking (Refs. 22, 42). Thus, rationale no. 3 is unable to explain even the broad trends in cracking behavior.

Evidence of a reduced solidification range in the presence of ferrite, the basis of rationale no. 4, was not observed in other portions of the study (Refs. 11-14). Neither the phase diagram (Refs. 1,2) nor the STEM data obtained suggests that the solidification ranges vary significantly. The more important factor may actually be the freezing point of the impurity-containing segregated liquid; this solidifies last and at a lower temperature than may be expected from the pure ternary diagram. In this case, rationale no. 4 may be similar to no. 2, although as discussed previously, rationale no. 1 cannot explain the cracking behavior.

Rationale no. 5 is based on the differences in partitioning of minor elements during primary ferrite solidification compared to that during primary austenite solidification. It is an often-referred-to concept that was studied by Arata *et al.* (Ref. 7). Astrom *et al.* (Ref. 31) have further suggested that the beneficial effect of primary ferrite solidification is that Mn is segregated to cell boundaries where it can react with S, forming spherical MnS and preventing the formation of iron or other liquid sulfide films. However, the behavior of ternary alloys in this study, with minimum minor elements such as Mn and Si, still shows that a large

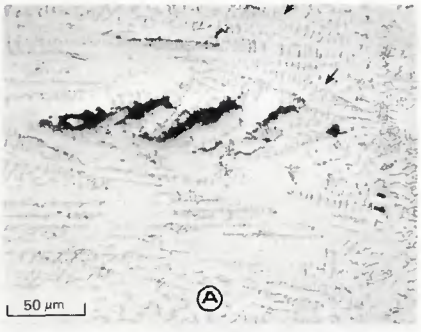

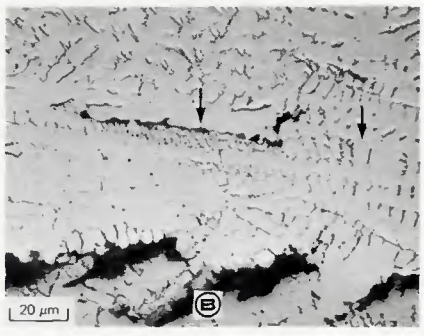

Fig. 17—Microstructures of Varestraint test specimens showing cracks in alloy 22-13 with ~.03% S: A—cracks associated with boundaries; B—higher magnification with crack along grain boundary adjacent to lathy ferrite

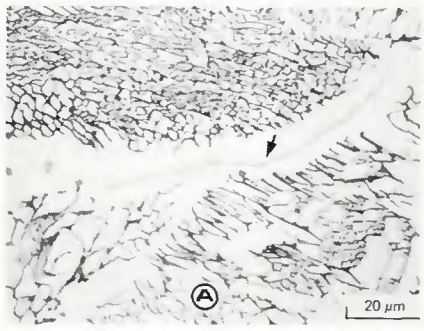

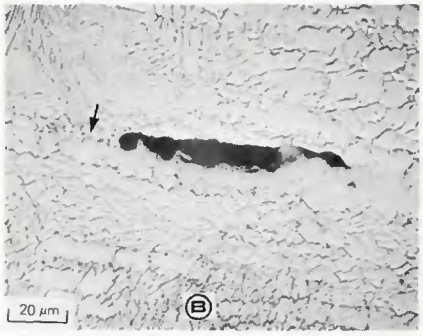

Fig. 18—Microstructures of Varestraint specimens of alloy 23-12: A—phosphide film along apparent boundary region (~0.2% P); B—crack along spherical sulfides (~0.16% S)

variation in cracking resistance occurs. Thus it seems that the partitioning of minor alloying elements (rationale no. 5) cannot be assigned a necessary role in explaining weld cracking behavior.

This result is not meant to suggest that minor elements, when present, do not play some beneficial, synergistic role with detrimental impurities such as phosphorus and sulfur. In fact, alloy design often incorporates this rationale in producing all austenitic weld wires which contain high levels of Mn.

Regarding rationales 6 to 8, it has been shown that hot cracks are nearly always associated with grain boundaries. Thus, it seems apparent that explanations dealing with the detailed nature of the boundaries in the presence or absence of ferrite, or differences in the boundaries resulting from various solidification modes, are most likely to be relevant in explaining hot cracking behavior. Since observations made in this study bear upon all three of these rationales, they are discussed together.

It was observed in this study that in primary austenite solidified structures, with no eutectic ferrite, grain boundaries straighten in order to lower surface energies—Fig. 15. This resulted in straight, smooth boundaries which could be easily wetted by liquid films resulting from impurities segregated to grain boundaries during solidification. Also, the migration of the grain boundaries would be expected to result in sweeping and at least somewhat further concentrating already high levels of impurities within the grain boundaries. The collected impurities would have been in many cases originally segregated along cell boundaries within the original solidified grain. However, this effect is probably small since the boundary does not appear to transverse more than about one cell spacing.

When some ferrite was present, it was observed that the grain boundaries were effectively pinned, as in the case of alloy 21-14 with a FN of 0.5. Also, the amount of cracking was reduced (alloy 21-14 compared to alloy 10-30), and the structure was more resistant to the formation of long cracks resulting from the liquid phosphide films. This fact is consistent with studies by Gooch and Honeycombe (Ref. 43) in which they observed that structures exhibiting large migrated grain sizes in all-austenite welds were more susceptible to weld cracking than fine-grained structures.

The exact reason for the beneficial effect of this small amount of ferrite is not clear. Studies by Hull (Ref. 22), and our results from 309 welds (Ref. 44), showed that cracks propagated almost entirely along ferrite-free grain boundaries and were arrested when they encountered ferrite within the boundaries. Also, our results in this study indicated that higher phosphorus levels could be tolerated (before long cracks formed) as eutectic ferrite content increased. Thus, more complicated crack paths (rationale no. 8) resulting from grain boundary pinning, lower surface energies of ferrite-austenite boundaries preventing wetting and acting as solid links within the austenite boundary (rationale no. 7), and the increased impurity solubility of ferrite (rationale no. 1) may all play a role in the beneficial effect of eutectic ferrite. As discussed below, however, either rationale no. 7 or 8 is likely dominant in reducing cracking.

It was apparent in this study that alloys which solidified as primary ferrite were the most resistant to cracking. However, there was also an increase in FN accompanying primary ferrite solidification in the alloys used for the study described here. Still, cracks were often more evident in the primary austenite regions of structures that had solidified in a mixed mode. Also, observations in other studies suggested that primary ferrite solidification, and not ferrite content, is most important in determining cracking resistance (Refs. 5,10,28,29).

The nature of the grain boundaries of primary ferrite solidified structures are of special interest. As discussed earlier, the boundaries were difficult to identify in primary ferrite solidified structures, partly because the boundaries are mobile in the austenite. Thus, in primary ferrite solidification in which no eutectic ferrite forms, the boundaries likely migrate into the cell structure and become incorporated with the ferrite-austenite interphase boundary.

In several regions in the micrographs of Figure 17, ferrite is roughly perpendicular to and appears to cross boundaries in a manner which would appear to impede severely the propagation of a boundary crack. Several of these regions are marked with arrows. The exact nature of all the boundaries is not clear. In fact, in some cases, what appears to be a boundary may only be the primary arm of skeletal ferrite. In several other cases, the grain boundaries incorporate or intersect considerable amounts of ferrite. Also, in Fig. 17 the cracks formed are short and blunt, indicating either that a large amount of strain was required for their formation and propagation or that they propagate with such difficulty that they are blunted after formation.

It is now clear that the beneficial effect of primary ferrite solidification is in some way related to the nature of the grain boundaries and additional discussion of the point is appropriate. Figure 19 contains schematics of intersecting solidifying grains, derived from Fig. 2. The boundaries of these grains are potential paths of hot cracks.

During solidification, low-melting segregates are entrapped along cell boundaries as spherical particles. Because of the lack of large-angle boundaries, these droplets cannot form films and propagate cracks. However, for 100% primary austenitic solidification in Fig. 19A, rather flat smooth crack paths exist. With the presence of low-melting segregated liquids and welding stresses, cracks easily form and propagate as long as the liquid phase wets the boundary. This schematic clearly depicts the case shown in the micrograph in Fig. 15C. Note also that the same result would be expected for 100% ferrite solidification, as has been demonstrated by Hull (Ref. 22).

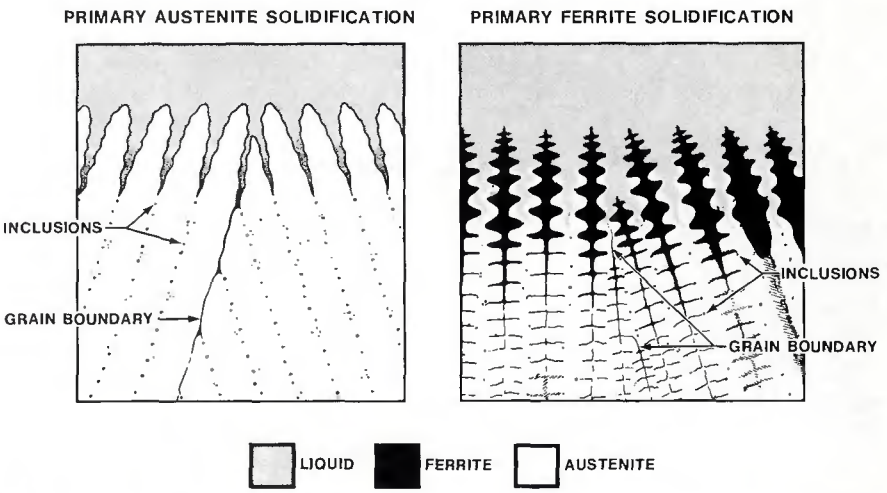

Fig. 19—Schematic representation of two intersecting solidifying grains. Left, primary austenite solidification showing the smooth crack path along an austenite grain boundary. Right, primary ferrite solidification showing complex crack path along boundaries due to the incorporation of the grain boundary along the $\delta - \gamma$ interface

The intersection of primary ferrite solidifying grains is somewhat more complicated as shown in Fig. 19B. The large ferrite-austenite boundary area within the two grains plays the same role in rationale no. 6 as bulk solubility of impurities in ferrite plays in rationale no. 1. Since even primary ferrite structures which were saturated in sulfur or phosphorus and contained large quantities of sulfides or phosphides were resistant to cracking, it is evident that rationale no. 6 explains cracking behavior no better than does rationale no. 1.

The grain boundary at the tip of the solidification front in Fig. 19B results from the intersection of secondary-austenite grains during peritectic solidification. As solidification proceeds, the austenitic boundary can migrate and become incorporated in the $\gamma - \delta$ interphase boundary as shown in the lower portion of Fig. 19. The migration of only the austenitic grain boundary may leave a string of particles or films along the original boundary region with no trace of the original boundary as shown in Fig. 18. As is evident schematically in Fig. 19, a crack could propagate only a short distance along the $\gamma - \gamma$ boundary before it would encounter the irregular $\gamma - \delta$ interphase boundary. This is different from the cracking scheme described by Matsuda *et al.* (Ref. 27) who did not identify the location of the grain boundaries, although their scheme somewhat resembles rationale no. 8.

The schematic shown as Fig. 19B also indicates the difficulty in metallographically determining the actual grain boundary location. This is because a large fraction of it is incorporated in the interphase boundary as previously noted. Also, the complicated crack path, or irregular surface of a crack, is more obvious. However, close examination of actual welds clearly shows some regions of $\gamma - \gamma$ boundaries, especially in lower ferrite content welds.

The difficulty of a crack propagating along a boundary, such as that shown in Fig. 19B, can be demonstrated with the aid of the TEM micrograph in Fig. 20. A boundary appears to be incorporated along skeletal ferrite as described above. For a crack to propagate along the boundary, it must either tear through the ferrite (which is presumably more difficult than boundary cracking) or propagate around the long path of the secondary ferrite arms, *i.e.*, rationale no. 8. Propagation along the interface would be difficult if these boundaries were not easily wetted by impurity phases, *i.e.*, rationale no. 7 in agreement with TEM observations showing the low energy configuration of the $\delta - \gamma$ interfaces. (A similar case would exist if the ferrite in Fig. 20 resulted from the intersection of two primary austenite solidifying grains, thereby leaving eutectic ferrite trapped between secondary austenite arms.)

It must be considered that the details of the schematic of primary ferrite solidification of Fig. 19 could have been drawn somewhat differently. For example, individual grains may solidify totally as ferrite while the grain boundary region, because of increased microsegregation caused by intersecting grain, may still solidify as a peritectic reaction. The grain boundary region would then still behave as described above, which appears to have occurred for the structures in Fig. 18.

It should also be noted that the grain boundary region may solidify completely as ferrite at sufficiently high Cr/Ni ratios; cracking could then occur along the ferrite grain boundary. However, if the $\delta \rightarrow \gamma$ transformation is initiated at a sufficiently high temperature, the formation of complex interfaces may retard crack propagation. Matsuda *et al.* (Ref. 32) have also suggested that cracking resistance is due to complicated crack paths, but it must be realized that the microstructure and nature of the boundaries will be considerably different at the high temperatures than that observed at ambient temperatures. The description of rationale no. 8 that was developed here is thus more complete than theirs.

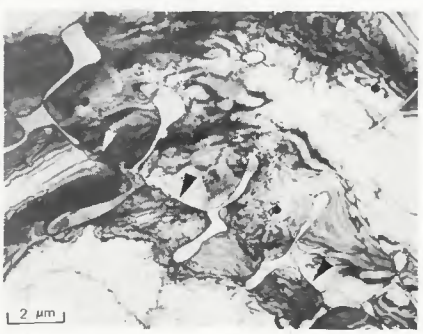

Fig. 20—Transmission electron micrograph showing ferrite across a grain boundary, demonstrating possibility of complex crack path

Summary

Fusion zone hot cracking is a possible consequence of the formation of low melting liquids resulting from microsegregation during weld metal solidification. These liquids will cause cracking along solidifying grain boundaries provided that:

1. The liquids can wet the boundaries.
2. The applied stresses, or stresses of thermal origin, are sufficient to separate the boundaries.
3. Insufficient liquid is available to heal the cracks formed.

A number of key experiments were conducted to understand the complex relationships between weld solidification, microstructural development and weld cracking resulting from liquid film formation. The findings are summarized below.

Single Phase Solidification

In primary austenite solidified welds with no eutectic ferrite, the grain boundaries were straight, or smooth, and easily wetted by the low melting segregated liquids containing phosphorus and sulfur. Little strain was required to produce weld hot cracks. A similar situation also exists for welds which solidify—and cool a considerable degree below the solidus temperature—completely as ferrite; however, the degree of wetting may be different.

Solidification as Primary Austenite with Eutectic Ferrite

Our studies indicate that when some eutectic ferrite forms during solidification, cracking is reduced because:

1. The grain boundaries are pinned and remain irregular, resulting in a more complicated crack path than in single phase austenitic solidification (which we have called rationale no. 8).
2. The lower surface energies of ferrite-austenite boundaries prevent them from being wetted by the impurity-containing liquid, and thus they act as solid links within the austenite grain boundaries and thereby prevent the boundaries from separating (rationale no. 7).
3. The increased solubilities of impurities in the ferrite during the last stages of solidification reduce the amount of low melting impurity-containing phase (rationale no. 1).

All of the above mentioned rationales may play a role in the beneficial effect of eutectic ferrite. However, it must be emphasized that in general—at least at low ferrite levels—these welds were much more susceptible to hot cracking than primary ferrite solidified welds.

Primary Ferrite Solidified Welds

Welds that solidified as primary ferrite were extremely resistant to cracking. This includes welds which solidify either as a peritectic or completely as ferrite, provided the ferrite-to-austenite transformation occurs at the grain boundaries at a temperature close to the solidus temperature. We have concluded in this study that:

1. Rationale no. 8, based on the role of the complex crack path encountered along the $\delta - \gamma$ boundary (modified as to the origins of the irregular boundaries as described above), is clearly a process which plays an important role in the high

degree of cracking resistance of these welds.

2. Rationale no. 7, based on the role of reduced wetting of $\delta - \gamma$ boundaries by liquid films compared to that of single phase boundaries, probably also plays a role which is consistent with our TEM observations.

Experiments remain to be done to separate these two rationales unequivocally. We also emphasize that the high impurity solubility in ferrite (rationale no. 1) probably contributes slightly to the performance of commercial alloys as may be the case with the partitioning of minor alloying elements (rationale no. 5). However, neither plays a major role or is necessary to cracking resistance.

The remaining four rationales are neither necessary nor sufficient for cracking resistance and at most must play a minor role. The four are:

- Rationale no. 2 – differences in the elevated temperature ductility of ferrite and austenite.
- Rationale no. 3 – differences in thermal expansion between ferrite and austenite.
- Rationale no. 4 – differences in the solidification range between primary ferrite and primary austenite solidified welds.
- Rationale no. 6 – ferrite resulting in a large internal surface area.

Acknowledgments

The authors gratefully acknowledge the assistance of R. Bell in experimental portions of this work. This work was funded by the Center of Joining of Materials at Carnegie-Mellon University and the U. S. Department of Energy, under contract number DE-AC04-76DP00789.

References

1. American Society for Metals. *Metals Handbook*, 8th ed., vol. 8, p. 424. Metals Park, Ohio.

2. Schurmann, E., and Brauchmann, I. 1979 (Nov.). *Archiv fur das Eisenhuttenwesen* 48:3-8.

3. Suutala, N., Takalo, T., and Moisio, T. 1979. *Met. Trans. A* 10A(4):512-514.

4. Fredriksson, H. 1972. *Met. Trans. A* 3:2989-97.

5. Masumoto, I., Tamaki, K., and Kutsuna, M. 1972. *Trans. JWS* 41(11):1306-1314.

6. David, S. A., Goodwin, G. M., and Braski, D. N. 1979. Solidification behavior of austenitic stainless steel filler metals. *Welding Journal* 58(11):330-s to 336-s.

7. Arata, Y., Matsuda, F., and Katayama, S. 1976. *Japanese Weld. Res. Inst. Trans.* 5(2):35-51.

8. Lippold, J. C., and Savage, W. F. 1980. Solidification of austenitic stainless steel weldments: part 2 – the effect of alloy composition on ferrite morphology. *Welding Journal* 59(2):48-s to 58-s.

9. Lippold, J. C. 1978. *An Investigation of Duplex Weld Solidification in Austenitic Stainless Steels.* Ph.D. thesis. Troy, New York: Rensselaer Polytechnic Institute.

10. Suutala, N., Takalo, T., and Moisio, T. 1980. *Metall. Trans. A* 11A(5):717-725.

11. Brooks, J. A. 1981 (April). *Composition Effects on the Microstructure and Cracking of Austenitic Stainless Steel Welds.* Ph.D. thesis. Pittsburgh, Pennsylvania: Carnegie-Mellon University.

12. Brooks, J. A., Williams, J. C., and Thompson, A. W. 1983. *Metall. Trans. A* 14A(1):23-31.

13. Brooks, J. A., Williams, J. C., and Thompson, A. W. 1983. *Metall. Trans. A* 14A(7):1271-1281.

14. Brooks, J. A., Williams, J. C., and Thompson, A. W. 1982. Solidification and solid state transformations of austenitic stainless steel welds. *Trends in Welding Research in the United States*, pp. 331-357. Metals Park, Ohio: American Society for Metals.

15. David, S. A. 1981. Ferrite morphology and variations in ferrite content in austenitic stainless steel welds. *Welding Journal* 60(4):63-s to 71-s.

16. Leone, G. L., and Kerr, H. W. 1982. The ferrite to austenite transformation in stainless steels. *Welding Journal* 61(1):13-s to 21-s.

17. Lyman, C. E., Manning, P. E., Duquette, D. J., and Hull, E. 1978. *Scanning Electron Microscopy*, vol. 1, pp. 110-213.

18. Scherer, R., Riedrich, G., and Hougardy, H. 1941 (May 6). *Welding rod.* U.S. patent 2,240,672.

19. Schaeffler, A. L. 1949. *Metals Progress*, vol. 56, p. 680.

20. DeLong, W. T., Ostrom, G. A., and Szumachowski, E. R. 1956. *Welding Journal* 35(11):521-s to 528-s.

21. Hull, F. C. 1973. Delta ferrite and martensite formation in stainless steels. *Welding Journal* 52(5):193-s to 203-s.

22. Hull, F. C. 1967. Effect of delta ferrite on the hot cracking of stainless steel. *Welding Journal* 46(9):399-s to 409-s.

23. Borland, J. C., and Younger, R. N. 1960. *British Welding Journal* 7:22-59.

24. Castro, R. J., and de Cadenet, J. J. 1974. *Welding Metallurgy of Stainless and Heat Resisting Steels.* Cambridge, England: Cambridge University Press.

25. Lundin, C. D., DeLong, W. T., and Sponds, D. F. 1975. Ferrite-fissuring relationship in austenitic stainless steel weld metals. *Welding Journal* 54(8):241-s to 246-s.

26. Brooks, J. A. 1975. Weldability of high N, high Mn austenitic stainless steel. *Welding Journal* 54(6):189-s to 195-s.

27. Brooks, J. A., and Lambert, F. J. Jr. 1978. The effects of phosphorus, sulfur and ferrite content on weld cracking of Type 309 stainless steel. *Welding Journal* 57(5):139-s to 143-s.

28. Takalo, T., Suutala, N., and Moisio, T. 1979. *Met. Trans A* 10(8):1173-1181.

29. Thier, H. 1976. *DVS-Ber.* 41:100-104.

30. Schurmann, E., and Brauchmann, I. 1979 (Nov.). *Archiv fur das Eisenhuttenwesen* 48:3-8.

31. Astrom, Loberg, B., Bingstsson, B. and Easterling, K. 1975. *Hot cracking and microsegregation in 18-10 stainless steel welds.* TULES 1975:09. Lulea, Sweden: Hogskolan I. Lulea.

32. Matsuda, F., Nakogawa, H., Uehara, T., Katayama, S., and Arata, Y. 1979. *Japanese Weld. Res. Inst. Trans.* 8(1):105-112.

33. DeLong, W. T. 1973. Technical note: calibration procedure for instruments to measure the delta ferrite content of austenitic stainless steel weld metal. *Welding Journal* 52(2):69-s to 73-s.

34. Solomon, H. D., and Levy, S. 1982. *Trends in Welding Research in the United States*, pp. 173-204. Metals Park, Ohio: American Society for Metals.

35. Blackburn, M. J., and Williams, J. C. 1967. *Trans. TMS-AIME* 239:287-288.

36. Goodwin, G. M. 1968 (June). *The Effect of Minor Elements on the Hot Cracking of Inconel 600.* Ph.D. thesis. Troy, New York: Rensselaer Polytechnic Institute.

37. Turner, P. W., and Lundin, C. D. 1970. Effect of hot cracking of uranium weld metal – part I. *Welding Journal* 49(12):579-s to 587-s.

38. Brooks, J. A. 1974. Effect of alloy modifications on HAZ cracking of A-286 stainless steel. *Welding Journal* 53(11):517-s to 523-s.

39. Nishiyama, Z. 1934. Sci. Report, Tohoku University, 23, p. 369.

40. Wasserman, G. 1933. *Archiv fur das Eisenhuttenwesen* 16:647.

41. Kurdjumov, G. V., and Sachs, G. 1939. *Z. Physik.* 64:325.

42. Kujanpaa, V., Suutala, N., Takalo, T, and Moisio, T. 1979. *Welding Research Inter.* 9(2):55-76.

43. Gooch, T. G., and Honeycombe, J. 1980. Welding variables and microfissuring in austenitic stainless steel weld metal. *Welding Journal* 59(8):233-s to 241-s.

44. Brooks, J. A., Williams, J. C., and Thompson, A. W. 1980. *Physical Metallurgy of Metal Joining*, R. Kossowsky and M. Glicksman, eds., pp. 117-136. Warrendale, Pennsylvania: Metallurgical Society of AIME.